

Higgs boson characterization and differential cross section measurements

Marcos Jiménez Larroy

2024/2025



GRADO DE FÍSICA. TRABAJO DE FIN DE GRADO

Tutored by:

Ana Rosario Cueto Gómez

Luis Pascual Domínguez

Since its discovery in 2012 in the Large Hadron Collider (LHC), the Higgs boson has been studied as it is intrinsically related to several still unexplained particle physics concepts and effects. In this project, data from proton-proton collisions with an energy of $\sqrt{s} = 13,6$ TeV at the center of mass produced in the LHC and collected by the ATLAS detector are analyzed, together with Monte Carlo simulations, to study the Higgs boson diphoton decay channel. The differential cross section with respect to the diphoton system transverse momentum is calculated and both the total Higgs production cross section and fiducial diphoton decay channel cross section are obtained, resulting in 53 ± 7 pb and 62 ± 10 fb respectively. This measures are in good agreement with the most recent experimental results (58 ± 6 pb and 74^{+16}_{-15} fb) and with the Standard Model predictions ($59,9 \pm 2,6$ pb and $67,6 \pm 3,7$ fb).

Contents

1	Introduction	3
1.1	The Higgs boson in high energy physics	3
1.2	Experimental concepts	4
1.3	The $H_0 \rightarrow \gamma\gamma$ process	4
1.4	Higgs Boson's production modes	6
2	ATLAS detector and the LHC	6
3	Data and Monte Carlo simulations	8
4	Event selection	9
5	Signal modeling	11
5.1	The Double-Sided Crystal Ball function	11
6	Background modeling	13
6.1	$\gamma\gamma$, γj and jj contributions	13
6.2	The Spurious Signal method	14
7	Experimental differential cross section and theoretical prediction	17
7.1	Unfolding	18
7.2	Uncertainties calculations	19
7.2.1	Experimental uncertainties	19
7.2.2	Theoretical uncertainties	20
8	Results	21
8.1	Higgs boson signal in the inclusive region	21
8.2	Differential cross section	22
8.3	Total cross sections	23
9	Summary and Conclusion	25
10	References	25
11	Appendix	28
11.1	Appendix A. Product cuts	28
11.2	Appendix B. Monte Carlo signal fitting results	32
11.3	Appendix C. Example of Spurious Signal method	34
11.4	Appendix D. Data fitting results	35
11.5	Appendix E. Comparison between NLO and NNLO	37

1 Introduction

1.1 The Higgs boson in high energy physics

The Standard Model (SM) is the theory that describes the fundamental interactions between elementary particles. This model includes two types of fundamental particles: fermions, which constitute matter, and bosons, who are the responsible of carrying the interactions. It has successfully explained three of the four fundamental interactions of nature: electromagnetic (felt by charged particles), weak interaction (felt by all the SM particles) and strong interaction (felt by quarks) over the last fifty years. The weak and electromagnetic forces are unified at high energy scales in the electroweak interaction and the Standard Model can be divided in this and the strong interaction, which is described by QCD (Quantum Chromodynamics). These fundamental particles acquire their masses through the Higgs mechanism, and as a result a new particle of spin zero is needed: the Higgs Boson. This boson is also responsible for a lot of different physical effects, and thus it constitutes a rich source of experimental material and physical knowledge.

The Large Hadron Collider was built with the ultimate goal of discovering the Higgs boson, predicted theoretically along the Higgs Mechanism during the 60s by Peter Higgs, Robert Brout and François Englert [1, 2]. Their theory was proved correct when the 4th of July of 2012 the ATLAS and CMS Collaborations announced the discovery of a particle consistent with the Higgs boson ¹ [3, 4]. Since its discovery, tons of precision measurements have been made in order to better understand its nature and implications.

More concretely, the Higgs Mechanism is responsible of the symmetry breaking of the electroweak force, resulting in the separation between the weak interaction and the electromagnetic force that is seen at low energies. This is the reason of the presence of massive bosons as the carriers of the weak interaction (Z^0 , W^+ and W^-) and of the masslessness of the photon as a carrier of the electromagnetic force. Thus, studying the Higgs boson and its mechanism has relevance in the behavior of other fundamental interactions.

Moreover, although the SM theory has proven to describe particle physics with great precision, it has 19 undetermined parameters that must be derived from experimental data; and out of those 19, 15 are intrinsic to the coupling of SM particles to the Higgs sector, showing the cruciality of studying it. Finally, the Higgs boson is related to several topics that have not been explained yet such as its composition, the CP violation², the concept of flavor, the presence of multiple particle generations, their masses, etc [5]. Thus, continuing the Higgs boson experiments is one of the best ways physicist have to find any evidence of their answers.

¹Its spin and parity had still to be measured to confirm the new particle.

²This is a way of quantifying the matter-antimatter asymmetry of the Universe.

1.2 Experimental concepts

The SM theory has been experimentally proved by studying particle collisions and the underlying interactions. To achieve this, experimental high energy physicists need to measure some magnitude that can be predicted by the SM and compared with results. One of the most important observables used for this purpose is the differential and total cross section of a defined process. This quantity can be intuitively described using a classical scattering experiment when a particle beam is directed towards a target. The total cross section is the ratio between the number of events (interactions between the beam particles and the target particles) per unit time and the product of the number of incident particles per unit time times the superficial density of target particles; and can be somehow understood as related to the probability of a certain reaction happening.

$$\dot{N} = \sigma \cdot \dot{N}_i \cdot n_T \equiv \sigma \cdot L \quad (1)$$

In Equation 1, σ is the total cross section and has units of area, \dot{N} and \dot{N}_i are the number of reactions and of incident particles per unit time respectively and n_T is the superficial density of target particles. The new variable L is the luminosity, and after integrating it in time is called ‘integrated luminosity’, an extremely used quantity in high energy physics (HEP). Its units are the inverse of an area. Although the common units for area are m^2 , it is useful to define another unit, called *barn*, which is more appropriate for the dimensions of high energy processes, and is related to m^2 as $1\text{ b} = 10^{-28}\text{ m}^2$.

The reaction events (or signal events from now on) can be divided according to different physical magnitudes, such as the solid angle (Ω) or the final momentum that the outgoing particles have (p_F). Thus, it is possible to define new magnitudes, called differential cross sections, which show the distribution of events with respect to a specific magnitude ($d\sigma/d\Omega$ is the most typical differential cross section). This observables are constantly measured in HEP experiments as they help to explore the different kinematic regimes of a given process and can be used as a test of the SM predictions. In this work, the differential cross section of the $pp \rightarrow H_0 \rightarrow \gamma\gamma$ process will be studied.

1.3 The $H_0 \rightarrow \gamma\gamma$ process

In order to study a particle, one should focus on a specific process where it is involved. In our case, the Higgs boson has a relatively large mass, which causes its lifetime to be quite short (around $1,6 \cdot 10^{-22}\text{ s}$ [6]). Thus, the detector will not be able to measure it directly, but the products of its disintegration. It then becomes relevant to choose wisely which decay channel to study. Some factors to take into account when choosing it are the resolution the detector could have measuring the particles involved, the amount of processes that could replicate the experimental signal and the probability of the process. This probability is called the branching ratio (BR).

In this project, the diphoton decay channel will be studied. If only the BR of the different decay channels is considered, this process actually has the second lowest probability of

happening of all possible decay channels (Figure 1), with a BR of $2,27 \cdot 10^{-3}$ at a Higgs mass of 125 GeV [7]. However, as mentioned before, this is not the only factor to take into account. All processes with higher BRs, except the $H_0 \rightarrow ZZ \rightarrow 4l$ channel, either include the production of gluon/quark jets or the production of neutrinos via the disintegration of a vector boson or τ leptons. The first type of processes are quite difficult to characterize as the experiment takes place in a proton-proton collider, where thousands of gluon/quark jets are already produced, making it challenging to distinguish them from the ones coming from the Higgs boson³. On the other hand, the remaining processes involve neutrinos, which are directly impossible to measure and the full invariant mass of the Higgs cannot be reconstructed. This leaves us with only two clean and with high resolution decay channels: the diphoton channel and the $H_0 \rightarrow ZZ$ channel, which was also used back in 2012 in the discovery of the Higgs boson.

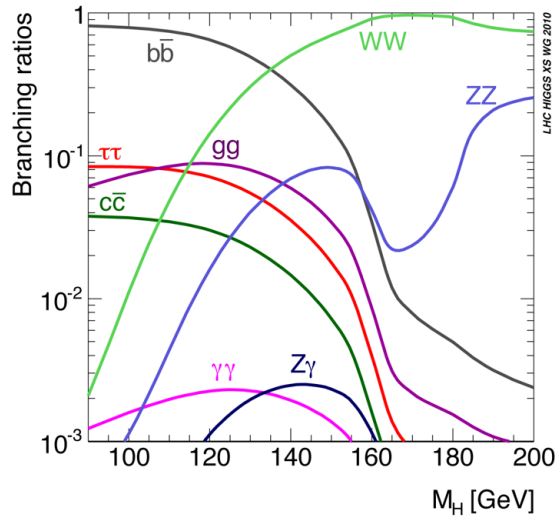


Figure 1: Higgs boson's decay channels branching ratios.

The strength of the coupling of particles with the Higgs boson is proportional to their mass. However, photons are massless particles, which would contradict the idea of the Higgs boson decaying into two of them because there is no coupling between these two particles. What really happens in a $H_0 \rightarrow \gamma\gamma$ process is that a loop of either W boson or top quarks (both massive particles) appears between the Higgs boson in the initial stage and the diphoton final stage. The Feynman diagrams for this processes are shown in Figure 2.

³Actually, the $b\bar{b}$ can be measured because of a small spatial separation between the vertices of the b quarks. However, it is much more difficult than the diphoton channel.

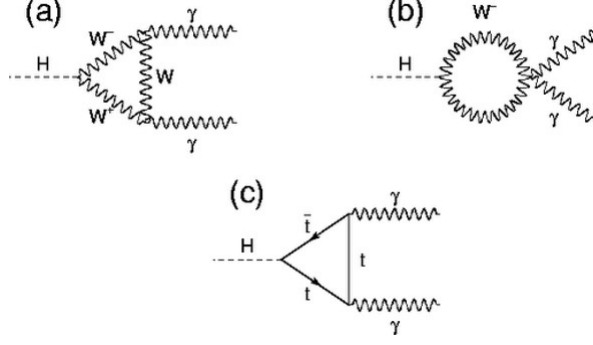


Figure 2: Feynman diagrams for the Higgs boson decaying in two photons.

1.4 Higgs Boson's production modes

The same way that the Higgs boson has different possible decay processes, it has different production modes. For the case of proton proton collisions, which is what will be studied, the most important one, responsible for about 87% of the Higgs boson productions, is called gluon-gluon fusion (ggF or ggH) and, as it names states, occurs when two gluons interact through a top quark loop to produce a Higgs boson. The second most important process is the vector boson fusion (VBF), where two quarks emit a vector boson and they merge to produce a Higgs boson, together with the two initial quarks. This process contributes with a 6,8% of the total production. Following in importance it is the WH/ZH process, in which the Higgs boson is emitted by a Z or W boson originally created in the merge of a pair quark-antiquark (4,0% in total) and the $t\bar{t}H/b\bar{b}H$ process, where a pair top-antitop/bottom-antibottom merges to yield a Higgs boson (0,9% each) [8]. This percentages can vary with the energy at the center of mass of the collision, which in our case is of $\sqrt{s} = 13,6$ TeV. Other subleading Higgs production modes like ggZH (Higgstrahlung coming from gluon fusion) or tH (in association with a top quark) have not been considered for this work.

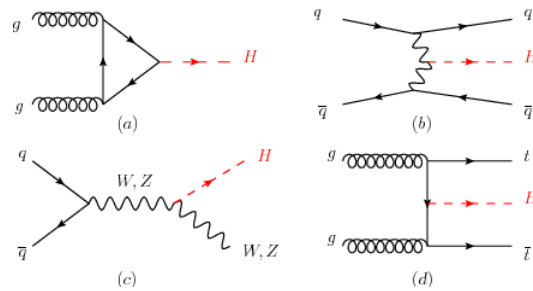


Figure 3: Feynman diagrams for the Higgs boson production modes. ggF (a), VBF (b), WH/ZH (c) and $t\bar{t}H$ (d).

2 ATLAS detector and the LHC

All the events that have been studied were proton-proton collisions collected by the ATLAS (A Toroidal LHC Apparatus) experiment, located in the Large Hadron Collider (LHC) in

Geneva, Switzerland. The LHC constitutes the largest collider ever built, with a 27 km long circumference. It is currently able to produce particle collisions with an energy at the center of mass (\sqrt{s}) of 13,6 TeV. As the particles that are collided in the LHC are protons⁴, which are made up by quarks, most of the processes will be dominated by QCD.

The ATLAS detector (44 meters long and 25 meters high) is designed with a layer architecture, where each of those layers is responsible for measuring a specific magnitude and type of particle. ATLAS uses a right-handed coordinate system with its origin at the nominal interaction point (IP) in the center of the detector and the z-axis along the beam pipe. The x-axis points from the IP to the centre of the LHC and the y-axis points upwards. The common r and ϕ cylindrical coordinates are used in the transverse plane. Regarding the third coordinate, instead of simply using θ as the classical polar angle a new quantity is defined called ‘pseudorapidity’ (η), whose dependence with θ is shown in Equation 2. Angular distance is thus measured in units of $\Delta R = \sqrt{(\Delta\eta)^2 + (\Delta\phi)^2}$ [7].

$$\eta = -\ln \left[\tan \left(\frac{\theta}{2} \right) \right] \quad (2)$$

The first layer is the inner detector, formed by a silicon pixel detector and a transition detector tracker. Surrounding this inner detector there is a superconducting solenoid creating a 2 T magnetic field. In this layer only electrically charged particles are measured. Moreover, their energy can also be measured by analyzing the curvature of their trajectories [9].

After this solenoid, there are two different calorimeters. The first and smaller one is the electromagnetic calorimeter, which uses liquid argon as scintillating material to measure the energy of electromagnetic interacting particles. The electromagnetic calorimeter will be key for our study as it is where photons and electrons are measured. It has three sections: two end-cap sections at the sides and one big cylindrical section. The latter is also divided in three layers filled with different width cells, where the energy left by the particle is measured.

By geometrical reasons, the electromagnetic calorimeter only covers the region with $|\eta| < 3,2$. Moreover, due to the separation between the sections, the regions where $1,3 < |\eta| < 1,5$; measurements are less efficient. After the electromagnetic calorimeter there is the hadronic calorimeter, which also measures energy deposition but it is specifically designed for neutral particles.

Lastly, due to the higher mass of muons and its high energies acquired in the collision, an extra layer was designed. This layer, called the muon chamber, consists of various precision tracking chambers located in the most external part of the ATLAS detector. A

⁴Heavy ions are also collided and studied in other detectors like ALICE, but in ATLAS proton-proton collisions are measured.

scheme of the layers of the detector and the particles that are measured in each of them is shown in Figure 4.

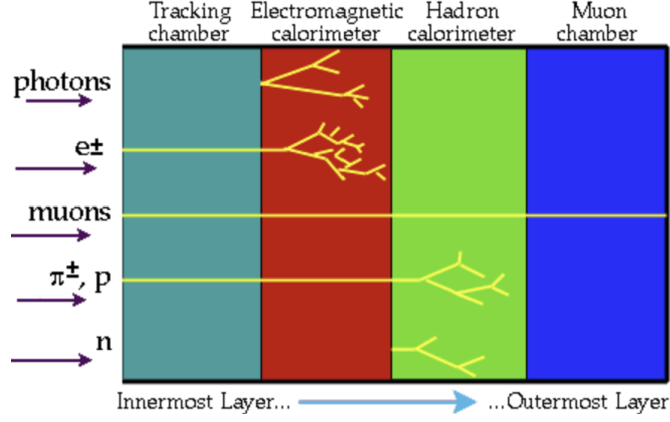


Figure 4: Scheme of the different layers present in the ATLAS detector and how each particle is measured

3 Data and Monte Carlo simulations

The experimental events that have been studied are events collected during the Run III period of the LHC, more precisely events from the 2022 and 2023 data-taking periods. The integrated luminosity is of $L = 58,98 \text{ fb}^{-1}$, where $31,40 \text{ fb}^{-1}$ correspond to the 2022 data and $27,58 \text{ fb}^{-1}$ from 2023 [10]⁵. Events were selected using a diphoton trigger that requests two online photon candidates with a transverse momentum (p^T) of 35 (25) GeV for the leading (subleading) photon when ordered in p^T ⁶.

For this analysis not only experimental data were used, but also Monte Carlo simulations. The use of Monte Carlo simulations is extremely useful as a way to compare the theoretical prediction with the experimental results. Both signal MC simulations and background MC simulations were used. The background simulated events are those where the final state of the event matches the one of the studied process but was not produced due to this process. Regarding the signal MC, all the simulated events included a Higgs boson decaying into two photons. They were divided by production mode, which enables the study of their characteristics individually.

The precision at which the matrix element amplitudes are computed in Monte Carlo generators is determined by the order of the strong coupling constant at which the perturbative analysis stops⁷. In HEP, it is common to call the first and simplest order as ‘Leading Order’ (LO) and the following ones just by adding ‘Next’ to the name whenever a new order is considered. For example, the ggH Monte Carlo events were calculated at

⁵A luminosity of 1 fb^{-1} means that an event with a total cross-section of 1 fb will statistically happen once.

⁶This magnitude is explicitly defined in Section 4

⁷The coupling constant of an interaction is a measure of its intensity.

NNLO (Next to Next to Leading Order) and the rest of the events were calculated at NLO (Next to Leading Order).

For the background simulations, two types of contributions were considered. One is irreducible background, where a pair of photons comes from QCD processes like $q\bar{q} \rightarrow \gamma\gamma$ and the other is the reducible background where a jet can be mis-identified as a photon, which usually happens when the jet contains neutral mesons like π_0 or η disintegrating in two photons.

4 Event selection

Before studying the Higgs Boson some filtering of events has to be done, as there are more than 10^9 events in the data and not all of them are $H_0 \rightarrow \gamma\gamma$ processes. To reduce the amount of events to look at, different selection criteria were applied. Every event that does not satisfy all of the requirements explained in this section was automatically discarded.

The first and most simple requirement is purely geometrical. Only the regions where photon and electron identification can be ensured are considered. Thus, the regions with $|\eta| > 2,37$ and $1,37 < |\eta| < 1,52$ are excluded [8].

Both photons must have a tight identification. The tight identification is related to the shape of the energy deposition that a particle leaves on the electromagnetic calorimeter, meaning that this shape is required to be quite narrow. This makes it more difficult for other processes to be mis-identified as a possible photon candidate. One usual example of such a process is the decay of a neutral meson, like a π_0 , into two photons. If these two photons are highly collinear, they might be identified as a single photon when hitting the electromagnetic calorimeter, as shown in Figure 5. However, by applying this cut, the process should be discarded. Although this constraint increases the purity of the signal, it also discards some correct events.

The photons must also be isolated. The reason for this constraint is that photons produced with the jets as part of hard hadronic processes want to be avoided as the target photons are produced completely isolated. To fully understand this requirement to magnitudes need to be introduced: the transverse momentum and the transverse energy.

When working with particle collisions in an accelerator like the LHC, the conservation of energy and momentum cannot be completely used, as there are particles that do not interact with the opposite beam. This makes it impossible to use the conservation of the momentum component which is parallel to the beam. However, it is useful to work with the perpendicular component. This component is called transverse momentum (p_T); and transverse energy (E^T) is defined using the common relativistic expression but replacing the total with the transverse momentum.

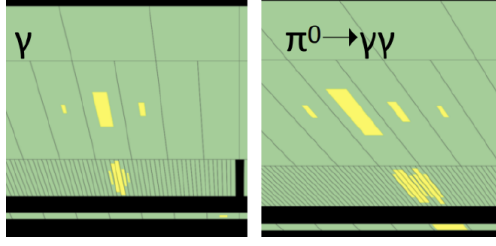


Figure 5: Example of a single photon energy deposit (left) and the energy deposit from two collinear photons coming from a π_0 disintegration. By requiring a tight ID, the right process could be discarded while the left one could be kept, although at a first glance they would look extremely similar.

$$p^T = \sqrt{p_x^2 + p_y^2} \quad ; \quad E^T = \sqrt{m^2 + (p^T)^2} \quad (3)$$

The transverse momentum is also a conserved quantity, which is zero at the beginning of the process and must be zero at the end. Thus, for example, a Higgs boson produced via ggH must have zero p^T , but if the production process was VBF , it could be different as two jets are also being produced.

To satisfy the isolation requirement, the transverse momentum of the incident photon is measured. Then, the total transverse momentum of all the tracks that have been recorded inside a cone of radius $R = 0,2$ in the (η, ϕ) plane are added and compared to the photon p^T . The same is done with the energy deposits in the calorimeters. The exact condition that the photons must satisfy in order to be considered isolated is the following [8]⁸:

$$\frac{p_{\Delta R=0,2}^T}{p_\gamma^T} < 5\% \quad \frac{E_{\Delta R=0,2}^T}{E_\gamma^T} < 6,5\%$$

In the case of massless particles, such as photons, $p^T = E^T$. If the lineal momentum of both photons is added, the transverse momentum of the diphoton system can be calculated ($p_{\gamma\gamma}^T$). By using the relativistic equation for energy, the invariant mass of the diphoton system ($m_{\gamma\gamma}$) can also be defined.

$$\vec{p}_{\gamma\gamma} = \vec{p}_{\gamma,1} + \vec{p}_{\gamma,2} \quad p_{\gamma\gamma}^T = \sqrt{(p_{\gamma\gamma}^x)^2 + (p_{\gamma\gamma}^y)^2} \quad m_{\gamma\gamma} = \sqrt{E_{\gamma\gamma}^2 - p_{\gamma\gamma}^2}$$

Using the fact that the Higgs boson has a mass of around 125 GeV, the selected photons should be quite energetic. More precisely, the leading photon (the most energetic one) must have a transverse energy ($p_{\gamma,l}^T$) of at least 35 GeV and the subleading one ($p_{\gamma,s}^T$) of at least 25 GeV. The total invariant mass must be between 105 GeV and 160 GeV. Additionally, their contribution to the invariant mass of the diphoton set must satisfy the following conditions [8]:

⁸While the first condition only isolated the photon with respect to charged particles, the second condition also considers neutral particles

$$\frac{p_{\gamma,l}^T}{m_{\gamma\gamma}} > 0,35\% \quad \frac{p_{\gamma,s}^T}{m_{\gamma\gamma}} > 0,25$$

This last criteria is called ‘relative p^T cut’ and it is arbitrary. Some other types of cuts can be used. In Appendix A a small analysis of an alternative criteria (‘product p^T cut’) is done. After applying all these constraints and conditions to the data, only a 0,013 % of the initial number of events satisfy the criteria. However, not all the events that have passed the cuts are $H_0 \rightarrow \gamma\gamma$ events; just diphoton events with these characteristics. A more detailed analysis must be done in order to detect the Higgs boson signal and thus be able to calculate its differential cross section.

Another interesting result to check is how many of the Monte Carlo signal events actually passed the cut. All of those events are $H_0 \rightarrow \gamma\gamma$ processes, but maybe the photons that are ejected do not satisfy some of the conditions. In Table 1 the efficiency by production mode result for our Monte Carlo simulations and from the 13 TeV simulations are compared [11]. All of them range between 29-38 %, enhancing the fact that, although the simulated events are all of interest, the characteristics of the photons emitted may not satisfy all of the imposed constraints.

Higgs Production Mode	ggH	VBF	$t\bar{t}H$	W_mH	W_pH	ZH
Efficiency 13 TeV	35,47	35,83	36,35	32,98	29,66	31,53
Obtained Efficiency	36,88	36,70	37,54	33,63	29,92	32,32

Table 1: Production modes efficiencies for 13 TeV simulations and calculated for the Monte Carlo Signal 13,6 TeV simulations.

It can be seen that the slightly higher value of the energy at the center of mass increases the efficiency of the event selection criteria.

5 Signal modeling

The first step in analyzing the experimental events that needs to be done is to describe the Monte Carlo simulations with simple analytical functions, which can then be easily compared with the distributions of the experimental events. The shape of both signal and background $m_{\gamma\gamma}$ distributions are the ones modeled.

5.1 The Double-Sided Crystal Ball function

The signal Monte Carlo invariant mass distribution is modeled using a *double-sided Crystal Ball* (DSCB) function, which is a generalization of a gaussian distribution whose external

tails are not necessarily symmetrical, as shown in the following equation [12]:

$$DSCB(m_{\gamma\gamma}) = N \cdot \left\{ \begin{array}{ll} e^{-t^2/2} & \text{if } -\alpha_{low} \leq t \leq \alpha_{high} \\ \frac{e^{-\alpha_{low}^2/2}}{\left[\frac{1}{R_{low}}(R_{low}-\alpha_{low}-t)\right]^{n_{low}}} & \text{if } t < -\alpha_{low} \\ \frac{e^{-\alpha_{high}^2/2}}{\left[\frac{1}{R_{high}}(R_{high}-\alpha_{high}-t)\right]^{n_{high}}} & \text{if } t > \alpha_{high} \end{array} \right\} \quad (4)$$

Where the normalization factor is N and there are six parameters to be adjusted:

- t is the reduced variable for the gaussian core, and it is defined using the two common gaussian parameters μ and σ as $t = (m_{\gamma\gamma} - \mu)/\sigma$.
- α_{low} and α_{high} are defined as positive and are values in the reduced variable (that is, with respect to t), where the gaussian center part ends and the power-law functions begin.
- The last free parameters are n_{low} and n_{high} , that correspond to the exponents of the power-law functions, both defined positive as well as the distribution will be descending from its highest value located in $m_{\gamma\gamma} = \mu$. R_{low} and R_{high} are just the quotients between the respective n and α .

After all the Monte Carlo signal simulated events have passed the event selection criteria, they are fitted to this function. In Figure 6a the general shape of a DSCB function is shown, together with our fit for the inclusive region $m_{\gamma\gamma}$ distribution (Figure 6b)⁹.

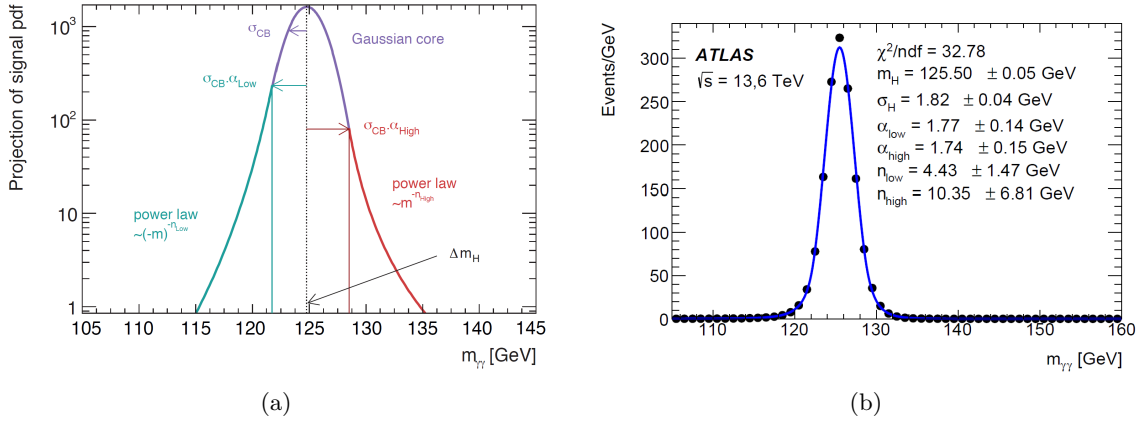


Figure 6: a) General shape of the DSCB function. b) Result for the fit to the $m_{\gamma\gamma}$ distribution in the inclusive region.

⁹The inclusive region term means that no other cuts were made, especially referring to the values of $p_{\gamma\gamma}^T$.

In order to calculate the differential cross section of this process with respect to the diphoton transverse momentum ($p_{\gamma\gamma}^T$), the events were binned based on this magnitude. For each of those $p_{\gamma\gamma}^T$ bins, the same procedure was made, and the fitted normalization constant is interpreted as the number of signal events in that $p_{\gamma\gamma}^T$ bin. Then, the differential cross section value for each bin can be obtained dividing the number of events by the width of the $p_{\gamma\gamma}^T$ bin and the total luminosity. The figures representing the fit and parameters for each of the bins have been added to Appendix B.

6 Background modeling

The goal of this section is to find a simple parametric function that can describe the background $m_{\gamma\gamma}$ distribution accurately. The strategy that is followed to model the background is quite different than with the signal modeling. First of all, as the Monte Carlo simulation only covers events where the two measured photons were real photons, it is necessary to estimate the contribution of processes where a jet could be mis-identified and counted as a photon while the other one is real (γj processes) or when both of them are mis-identified jets (jj processes). After this contribution is taken into account, the background events are separated into $p_{\gamma\gamma}^T$ bins just as the signal events were in the previous section. For each of the bins, an analytic function is chosen from a pool of preselected functions to fit the background $m_{\gamma\gamma}$ distribution, based on a method called Spurious Signal Method, which will be explained in section 6.2. As the $m_{\gamma\gamma}$ distribution is expected to be a descendant function, only these type of functions are added to the pool.

6.1 $\gamma\gamma$, γj and jj contributions

Due to computational reasons, the Monte Carlo simulations only contain information about events where both measured photons are indeed photons, although it is possible that a jet is identified incorrectly as a photon. As this process is not frequent, simulating events until a notorious statistical amount of these type of events is achieved would require a high quantity of computational power. In the ATLAS experiment, to take these contributions into account, it is assumed that the shape of the $m_{\gamma\gamma}$ distribution for γj events is the same in different locations of the phase space (more precisely, for example, in the non-tight region). This shape is extracted from experimental data. Knowing the γj distribution in this ‘control region’ it can be brought back into the phase space region of interest and compared to the Monte Carlo distribution. Finally, this Monte Carlo distribution is reweighted to account for the change in normalization and shape of the $m_{\gamma\gamma}$ distribution, obtaining a ratio between the nominal $\gamma\gamma$ distribution and the new distribution. This ratio will be applied to the Monte Carlo distribution for every $p_{\gamma\gamma}^T$ bin. It has been studied that the jj contribution, where both jets are mis-identified as photons is negligible [11].

As it can be seen in Figure 7, the γj is not a crucial part of the distribution, but it already has an importance of around 5% for high values of $m_{\gamma\gamma}$. In general, the γj distribution will be steeper than the $\gamma\gamma$ distribution in the sense that it will contain more events at lower $m_{\gamma\gamma}$ values and less at higher $m_{\gamma\gamma}$ values. This is because the purity of the

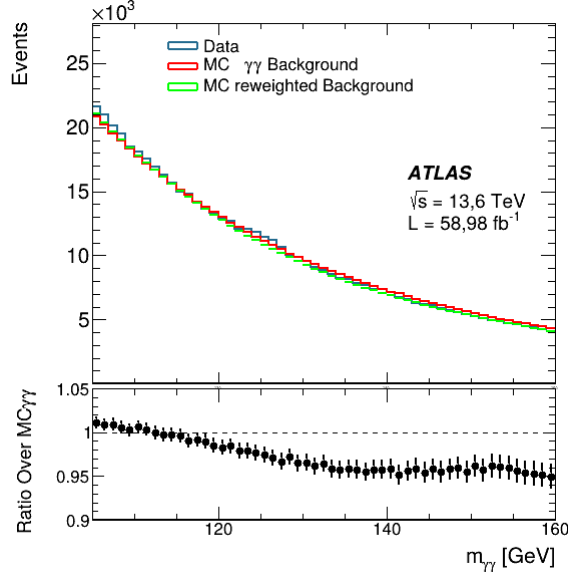


Figure 7: Comparison between the nominal $\gamma\gamma$ Monte Carlo simulation distribution and the reweighted background distribution once the γj event contributions have been considered, using the experimental distribution sidebands as a template.

photon identification increases with the energy of the received photon, and thus at higher energies it becomes more difficult for a jet to be mis-identified as a photon.

6.2 The Spurious Signal method

Once the background $m_{\gamma\gamma}$ distribution is ready, it is time to find an analytic function to represent it. To do this, various options from a pool of functions are subjected to the spurious signal test. The chosen functions were the following:

- Power-Law Function: $f(m_{\gamma\gamma}) = m_{\gamma\gamma}^\alpha$
- Bernstein polynomial of order 3: $f(m_{\gamma\gamma}) = B_3(m_{\gamma\gamma}) = \sum_{i=0}^3 c_i \cdot b_{i,3}$ with $b_{i,3} = \binom{3}{i} m_{\gamma\gamma}^i (1 - m_{\gamma\gamma})^{3-i}$
- Exponential Function of First Order Polynomial: $f(m_{\gamma\gamma}) = e^{c \cdot m_{\gamma\gamma}}$
- Exponential Function of Second Order Polynomial: $f(m_{\gamma\gamma}) = e^{c_1 \cdot m_{\gamma\gamma} + c_2 \cdot m_{\gamma\gamma}^2}$
- Exponential Function of Third Order Polynomial: $f(m_{\gamma\gamma}) = e^{c_1 \cdot m_{\gamma\gamma} + c_2 \cdot m_{\gamma\gamma}^2 + c_3 \cdot m_{\gamma\gamma}^3}$

The objective of this method is to estimate the bias added to the analysis by selecting an arbitrary function to fit the Monte Carlo background distribution. To achieve this, the Monte Carlo background template for every $p_{\gamma\gamma}^T$ bin is fitted to a linear combination of one of these functions and a signal function, which in this case would be a Double-Sided Crystal Ball function. The parameters for the signal function are taken directly from the results obtained in previous fits (Section 5), except for the normalization parameter,

which is left as free. Thus, the final function that would be fitted to the Monte Carlo background-only distribution will have the following structure:

$$F(m_{\gamma\gamma}) = N_{bkg} \cdot f(m_{\gamma\gamma}) + N_{SS} \cdot DSCB(m_{\gamma\gamma}) \quad (5)$$

Where $f(m_{\gamma\gamma})$ is any of the previously presented functions and N_{SS} , which is the spurious signal, is itself a measure of the bias estimation and is expected to be one of the leading contributions to the systematic error of the analysis. A pictorial and exaggerated example of the concept is shown in Figure 8. Once this fitting process has been completed for all of the five options, the conditions that must be met in order for a function to be selected as the best option to represent the background $m_{\gamma\gamma}$ distribution are [11, 12]:

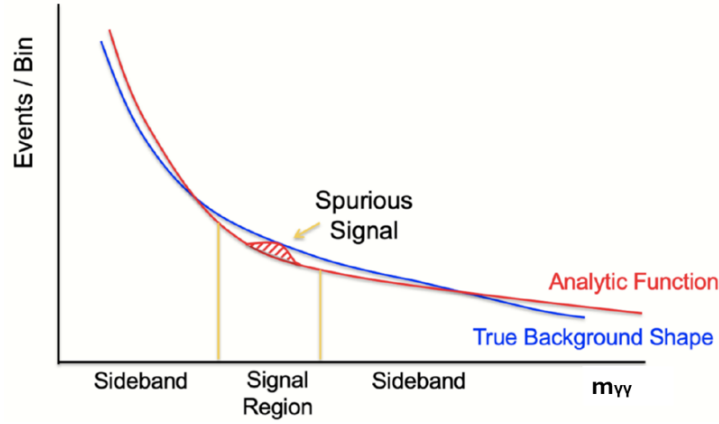


Figure 8: Basic illustration of the spurious signal. The blue line represents the Monte Carlo background-only distribution while the red line represents the analytical function chosen plus the signal distribution located in the signal region. The spurious signal itself is the normalization coefficient accompanying the signal distribution, which in an ideal case where analytical function and background-only distribution were identical and without statistical noise, would be zero [13].

- $N_{SS} < 15\%$ of the number expected signal events
- $N_{SS} < 20\%$ of the background uncertainty
- p-value is larger than 1%

The first condition is probably the most easily understandable of the three. As the function is fitted to a background-only distribution, there should be no sign of signal events. Thus, if the chosen function is a good selection, the coefficient N_{SS} should be negligible. In order to quantify this idea, the limit of 15 % of the expected signal events, which are obtained from the Monte Carlo signal simulations, is used.

While the first condition aims at the absolute number of signal events resulting from the fitting process, the second condition is related to the relative relevance of the coefficient N_{SS} obtained and the overall background distribution. For binned distributions and raw events, the bin error is usually calculated as the square root of the number of events in the bin. In this case, the background uncertainty is calculated as the square root of the number of background-only events in the signal region (from 120 to 130 GeV). For the same N_{SS} value, if the underlying background-only distribution is smaller, the relevance of N_{SS} increases. In this case, the desired effect is the opposite: making the relative relevance of the spurious signal as low as possible (more specifically, at least less than 20% of the background uncertainty). This idea is visually explained in Figure 9.

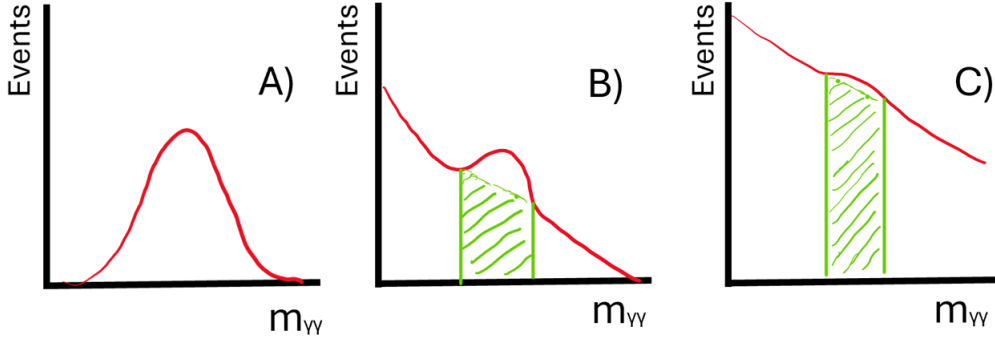


Figure 9: These three sketches represent functions $F(m_{\gamma\gamma})$ with the same N_{SS} coefficient. In figure A), no background function exists and thus this function is of course not valid. In figure B), some background function exists. However, the signal contribution is still large in comparison with it, and this can be measured by comparing N_{SS} with the background error (square root of the events in the green area). Figure C) is the desired output. In this case, the signal contribution is almost negligible in comparison with the background error and background events in the signal region, and thus this N_{SS} that has been fitted could perfectly be due to statistical fluctuations.

Regarding the last condition, it is necessary to introduce the statistical concept of p-value. In a more formal way, the p-value represents the probability of obtaining certain results considering that the null hypothesis (the hypothesis that is being tested) is true. In this case, the null hypothesis would be “the background-only distribution can be fitted to the function $F(m_{\gamma\gamma})$ once the parameters have been optimized”. The fact that the obtained p-value is large enough (in our case more than 1 %) means that whatever the obtained spurious signal is, it is compatible with a background-only distribution’s statistical fluctuations. If the p-value was lower than this limit, it would mean that the fitted function is finding too much of a signal for it to be compatible with a background-only distribution.

If more than one function of the proposed ones fulfills these three conditions, the one with the lowest amount of free parameters will be used. The functions with less free

parameters are the power function (*Power*) and the first order polynomial exponential (*ExpPol1*) with only one parameter, followed by the second order polynomial (*ExpPol2*, with two), the third order polynomial exponential (*ExpPol3*, with three) and the Bernstein polynomial (*Bernstein*, with four). In Table 2 the selected functions for each bin are shown, together with the obtained spurious signal and other relevant quantities for the analysis.

Bin Number	$p_{\gamma\gamma}^T$ (GeV)	Function	N_{SS}	$N_{expected}$	Background uncertainty
0	0-6	Bernstein	2,324	83,417	59,127
1	6-12	ExpPol3	13,685	167,805	77,631
2	12-18	ExpPol3	12,593	168,445	74,976
3	18-24	ExpPol3	6,818	147,158	70,367
4	24-30	ExpPol3	3,154	123,663	64,736
5	30-36	ExpPol3	2,873	102,871	59,312
6	36-45	ExpPol3	13,337	123,312	64,621
7	45-54	ExpPol1	11,984	94,531	49,575
8	54-66	ExpPol3	12,401	94,901	54,922
9	66-90	ExpPol2	11,715	121,134	57,293
10	90-114	ExpPol2	2,044	69,751	36,534
11	114-138	Power	2,084	43,825	22,201
12	138-192	ExpPol1	0,644	52,886	19,675
13	192-312	ExpPol1	0,373	34,314	11,725
14	312-624	Power	0,376	8,427	4,125
15	624-1500	ExpPol1	0,027	0,367	0,682

Table 2: Spurious Signal analysis results for each of the $p_{\gamma\gamma}^T$ bins.

It is important to clarify that this method is appropriate when the original background-only distribution has enough data and relatively small statistical fluctuations. Thus, as for the high $p_{\gamma\gamma}^T$ region there are less events than in the lower region, the bins become wider as we increase the value of the $p_{\gamma\gamma}^T$. An example of the results obtained for an arbitrary bin is displayed in Appendix C.

7 Experimental differential cross section and theoretical prediction

Once an analytic function that models the background $m_{\gamma\gamma}$ distribution correctly is found and the shape of the signal has been modeled with the DSCB function, the differential cross section for the $H_0 \rightarrow \gamma\gamma$ process can be calculated. The way to obtain the final result is the following. For each of the $p_{\gamma\gamma}^T$ bins presented in Table 2, the experimental data will be fitted by a function that follows the same structure as the one in Equation 5. The parameters for the signal term will be taken from the Monte Carlo signal simulations, leaving the normalization (which will now be called N_S) as a free parameter. On the background side, only the function structure will be used from the results shown in Table 2, while all the function parameters will remain free.

Once the function has been fitted, the final N_S coefficient will be the number of signal events detected. To finally obtain the expression of the differential cross section, this number of signal events must be divided by the integrated luminosity of the experimental data ($L = 58,98 \text{ fb}^{-1}$) and by the width of each bin. The fit results for each $p_{\gamma\gamma}^T$ bin are gathered in Appendix D.

$$\left(\frac{d\sigma}{dp_{\gamma\gamma}^T}\right)_i = \frac{N_{S,i}}{L \cdot \Delta p_{\gamma\gamma,i}^T} \quad (6)$$

7.1 Unfolding

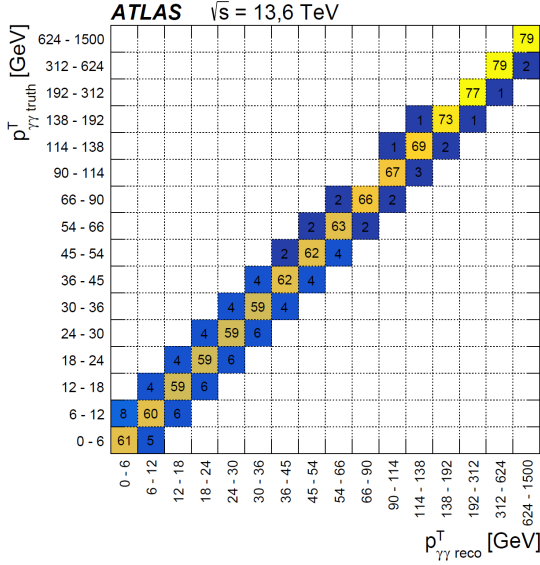
The events that the experimental high energy physicists measure directly are said to be in the ‘reconstruction level’, which means that the effects that the detector itself has in the particles are already included. However, pure theoretical predictions do not include the consequences of having a detector when measuring. Thus, it becomes relevant to find a way of going back to the process stage where the detector has not interfered yet. This is called the ‘particle’ or ‘truth level’. Now there are two different variables accounting for the transverse momentum of a particle: $p_{\gamma\gamma, reco}^T$ and $p_{\gamma\gamma, truth}^T$, each of them referred to their respective level. Another relevant reason to focus on the truth level is that only big experimental collaborations have the resources to create a fully detailed approximation of the detector for their Monte Carlo simulations while smaller ones’ simulations may not be as precise. Moreover, when high energy physicists want to compare results from the same process but measured in different detectors, this is a great way of eliminating the possible effects that each individual detector may have on the data. This process of going from the current ‘reconstruction level’ to the more purely physical ‘truth level’ is called unfolding,

To obtain the truth level results, Monte Carlo simulations are used again. In this case, the event selection criteria are the same as the ones explained in Section 4 except from the isolation conditions, which now only include charged particles when calculating the energy in the ΔR cone [7]¹⁰. For the theoretical prediction, the process to obtain the differential cross section is exactly the same as the one explained before, and the $p_{\gamma\gamma, truth}^T$ bins have been chosen to be the same as the previous ones. On the other hand, this obviously cannot be done with our experimental data. In order to do the unfolding, the results from the Monte Carlo simulations are analyzed and extrapolated to the experimental data.

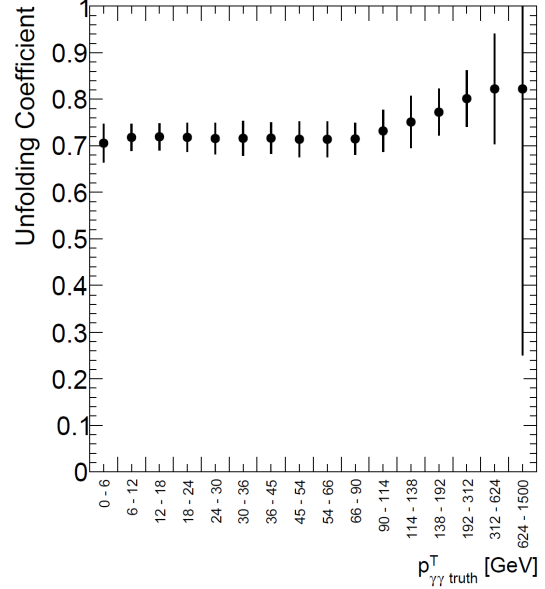
Two possible effects must be taken into account. The first and simpler one is that the number of events passing the fiducial selection cuts is greater than those passing the reconstruction cuts. The second effect has more complex consequences and it is related to $p_{\gamma\gamma}^T$ migrations. When an event satisfies both the fiducial and the reconstruction criteria, nothing assures that its $p_{\gamma\gamma, reco}^T$ and its $p_{\gamma\gamma, truth}^T$ will be in the same $p_{\gamma\gamma}^T$ bin, and thus migrations between bins are common. This effect could complicate the unfolding process as not all the events that were counted in one $p_{\gamma\gamma, reco}^T$ bin will belong to the same $p_{\gamma\gamma, truth}^T$ bin. Nevertheless, if the migration is small in comparison with the number of events that

¹⁰The events that satisfy these event selection conditions are said to be ‘fiducial’ or to be in the ‘fiducial region’

do remain in the same bin, the approximation of considering no $p_{\gamma\gamma}^T$ migration can be made. Figure 10 represents the $p_{\gamma\gamma}^T$ migration/response matrix and the final unfolding coefficient for each bin, which state for the quotient of the number of events in a $p_{\gamma\gamma, reco}^T$ bin and in the same $p_{\gamma\gamma, truth}^T$ bin.



(a)



(b)

Figure 10: a) Response matrix from Monte Carlo simulations for the diphoton system transverse momentum $p_{\gamma\gamma}^T$. Each component represents the probability in % of a generated event in a $p_{\gamma\gamma, truth}^T$ bin to fall into a $p_{\gamma\gamma, reco}^T$ bin. Values below 1% are not shown for more clarity. b) Unfolding coefficient for each $p_{\gamma\gamma}^T$ bin considering the previous matrix diagonal.

As shown in Figure 10a, the response matrix is almost diagonal, with some small $p_{\gamma\gamma}^T$ migrations only noticeable between neighbor bins. Thus, the previously commented approximation could be valid for the scope of this work. It is clear than the efficiency results increase with the $p_{\gamma\gamma}^T$. This is something expected for two different reasons. First of all, the bins for high $p_{\gamma\gamma}^T$ values are wider, and thus the probability of an event having a $p_{\gamma\gamma}^T$ close to the bounds of the bin is lower. Secondly, when photons are highly energetic it is easier for them to go through the detector without losing much of their $p_{\gamma\gamma}^T$, and thus it is highly probable that their $p_{\gamma\gamma, reco}^T$ matches the $p_{\gamma\gamma, truth}^T$. To finally obtain the true experimental differential cross section the obtained results must be divided by the unfolding coefficient values from Figure 10b.

7.2 Uncertainties calculations

7.2.1 Experimental uncertainties

There exist two different uncertainties sources for the experimental results. First of all, there are statistical uncertainties, related to the fitting error of the $F(m_{\gamma\gamma})$ function to

the experimental data or the efficiency of the different systems that are involved in the event selection criteria. Secondly, there are systematic uncertainties. In this case, the experimental statistical error will mostly come from the fitting error of the parameter N_S and the most noticeable systematic error is expected to be the spurious signal detected when choosing which function to choose for each bin. The statistical error is found to be much more important than the systematic for this case, and thus the later will be discarded for the final results.

7.2.2 Theoretical uncertainties

When simulating the $H_0 \rightarrow \gamma\gamma$ events, the SM including the Higgs boson with a mass of around 125 GeV is used. However, the calculations needed to simulate these events are not analytical and are calculated using approximations and numerical methods. In order to obtain stable results, different scales need to be introduced in the computation of the scattering amplitudes needed for the Monte Carlo simulations. The two most important ‘manually included’ parameters of the simulations are the refactorization and the renormalization scale.

The most intuitive one is the refactorization scale. As it was commented in Section 3, the Monte Carlo simulations are calculated using a perturbative analysis. However, Quantum Chromodynamics (QCD) cannot be resolved perturbatively at all energies. In the low energy regime, the particles taking part in the processes (quarks and gluons, also called partons) are confined inside the protons due to the higher value of the coupling constant of QCD (α_s) and QCD is non-perturbative. For higher energies, the partons can be considered ‘asymptotically free’. This is key in order to calculate cross sections as in this regime (perturbative regime) the non-perturbative dynamics of partons inside the proton and the partonic cross section of the process (e.g. $q\bar{q} \rightarrow H_0$) can be factorized¹¹. The limit that one chooses when deciding which energies correspond to the perturbative regimen and which correspond to the non-perturbative one is arbitrary (μ_F^2), which is usually set as $\mu_F = Q$ [14]¹².

The second variational scale is the renormalization scale. This has a more theoretical origin, and it is commonly used in quantum field theories to avoid divergences when doing the calculations. As a consequence of the introduction of this renormalization scale (μ), all renormalized quantities such as the coupling constants of the interaction develop an explicit dependence on μ . As this scale is arbitrary, it must happen that the underlying physics do not depend on it. This concept gives birth to the ‘Renormalization Group Equations’. In QCD these equations are solved by defining a *running coupling* ($\alpha_s(Q^2)$)[14].

The independence of the physical results with μ is only completely true when all the terms of the perturbative series are considered. In the Monte Carlo the ggF processes

¹¹In this process the parton distribution functions (PDFs), which represent the quark distribution inside a proton depending on the relative momentum that each has, also has huge relevance.

¹² Q^2 here represents the exchanged four-momentum between both interacting quarks.

are considered at NNLO¹³ and the rest at NLO, so some variations can be seen when these scales are varied, as the effects of the renormalization scale are usually greater at low perturbative orders. Both the renormalization scale and the refactorization scale are varied by the same factors (2 and 0,5) and the effects are measured. Moreover, seven combinations are considered (discarding when one is doubled and the other is halved), where the one with both unaltered is our reference¹⁴.

Lastly, for the ggF processes, another small variation is made. The Monte Carlo sample has an NLO precision for Higgs plus jet processes, but a reweighting is applied to achieve NNLO accuracy for inclusive variables. This makes the uncertainties calculations harder. To calculate them the relevance of the NNLO terms was varied (one overestimating it and one underestimating it), estimating the theoretical error that is committed by not adding all the other terms of the perturbative series.

As shown in Section 1.4, ggF is responsible for about 87 % of the Higgs boson productions. Thus, only the ggF contribution was considered for the theoretical error. Finally, as there are in total nine different ways of varying these parameters, nine different differential cross sections will be calculated. Given that there is an intrinsic correlation among all these variations, the highest differential cross section value at each $p_{\gamma\gamma}^T$ bin has been considered as the superior uncertainty and the lowest differential cross section value as the inferior, obtaining an envelope around the theoretical obtained value that will represent the theoretical uncertainty for each $p_{\gamma\gamma}^T$ bin.

8 Results

8.1 Higgs boson signal in the inclusive region

After following all the steps previously explained, the Higgs boson signal can be differentiated from the background events. To calculate the differential cross section, which is presented in the next subsection, the process is repeated for every $p_{\gamma\gamma}^T$ bin. However, an interesting insight from what can be expected for each bin can be obtained if the process is done for the inclusive region (without categorizing events by their $p_{\gamma\gamma}^T$). This result is shown in Figure 11. For the fitting, the Monte Carlo results for the inclusive signal simulations were used; except for the normalization, which was left as a free parameter. The fact that the DSCB function centered in 125 GeV matches correctly the observed data indicates that the mass of the Higgs boson being considered is adequate.

¹³The reason for this extra order for ggF processes is that as the order is increased, new processes appear which are not just refinements of previous processes, and so NNLO needs to be considered in order to have some precision when predicting the final cross section.

¹⁴This method is usually called a 7-point variation. If the two cases that have been discarded were considered it would be a 9-point variation.

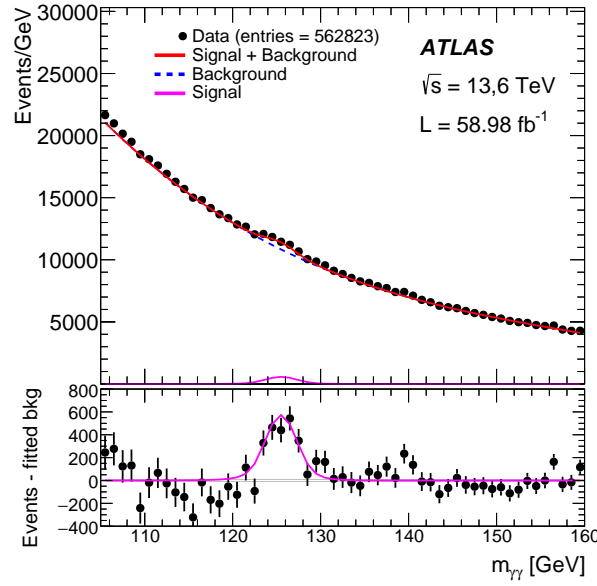


Figure 11: Results for the analysis of the inclusive region. The $m_{\gamma\gamma}$ experimental distribution is presented in the upper graph together with the fitting results of the background distribution, signal events and the sum of the two. On the lower graph the difference between the experimental events and the background fit is graphed, showing a clear signal around the Higgs boson's mass.

8.2 Differential cross section

The second and most important result is the differential cross section of the $pp \rightarrow H_0 \rightarrow \gamma\gamma$ process, calculated using Equation 6. As shown in Figure 12a, the experimental results match the theoretical predictions in a reasonable way, although there are some bins where the experimental events detected are less than what the theory predicts. This effect is mostly related to the statistical fluctuations that usually appear in the experimental $m_{\gamma\gamma}$ distribution for the diphoton system when the events are categorized by $p_{\gamma\gamma}^T$. It is also important to highlight that the width of the bins was decided so that the characteristic peak located between 5 and 20 GeV in the differential cross section, known as the Sudakov peak [15], could be resolved. This, however, increases the statistical error and fluctuations in the data.

It is interesting to compare this results with the Run II results obtained by the ATLAS Collaboration [7]. In this analysis a luminosity of $L_{Run\ II} = 139\ fb^{-1}$ was used. As shown in Figure 12b, the ATLAS Collaboration also obtains a higher than expected amount of signal events close to the Sudakov Peak and some experimental results which do not completely absorb the theoretical prediction in their error bars. Either way, both experimental distributions follow the general structure of the theoretical differential cross section and, excluding some specific bins, the results match the predictions, demonstrating again that

the Standard Model as it has been introduced in the Monte Carlo simulations constitutes a decent theory to explain the $pp \rightarrow H_0 \rightarrow \gamma\gamma$ process differential cross section, at least with the precision of current experiments.

As the differential cross section in high $p_{\gamma\gamma}^T$ bins cannot be seen, it is shown in logarithmic scale in Figure 13. It is interesting to show the shape of both NLO and NNLO distributions in this region because the differential cross section starts to be sensitive to mass effects of the particles than intervene in the loop processes (those considered at higher orders). This makes the high $p_{\gamma\gamma}^T$ region relevant because it could be sensitive to new physics, such as a fourth family of massive fermions; which in case of existing could have some effects here. The differences between both are further explained in Appendix E.

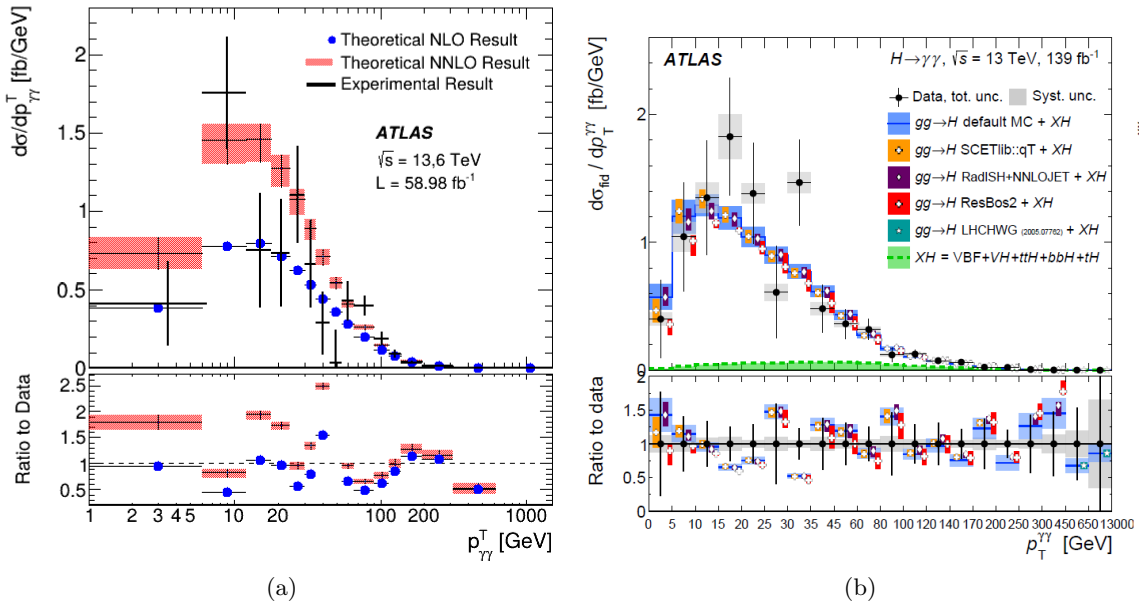


Figure 12: a) Differential cross section with respect to $p_{\gamma\gamma}^T$ for the $pp \rightarrow H_0 \rightarrow \gamma\gamma$ process. The red boxes represent the theoretical prediction considering NNLO for the ggH events, with its respective error band. The blue points represent the theoretical result considering only NLO for ggH events. The clear difference between them enhances the importance of considering higher orders in this simulations, as commented in Section 7.2.2. The black crosses represent our experimental results. b) Differential cross section with respect to $p_{\gamma\gamma}^T$ for the $pp \rightarrow H_0 \rightarrow \gamma\gamma$ process results for the ATLAS Collaboration [7] .

8.3 Total cross sections

Lastly, we can integrate the differential cross section in the $p_{\gamma\gamma}^T$ variable to obtain the total cross section. In 2024 the ATLAS Collaboration released their results using $\sqrt{s} = 13,6$ TeV events and obtained a total cross section of $58,2 \pm 8,7$ pb [15]. To get to this result, the total experimental cross section of our $pp \rightarrow H_0 \rightarrow \gamma\gamma$ process is divided by the branching ratio of this decay channel, which was presented in Section 1.3. Lastly, the Monte Carlo results from Table 1 are used to obtain an estimation of the efficiency of the

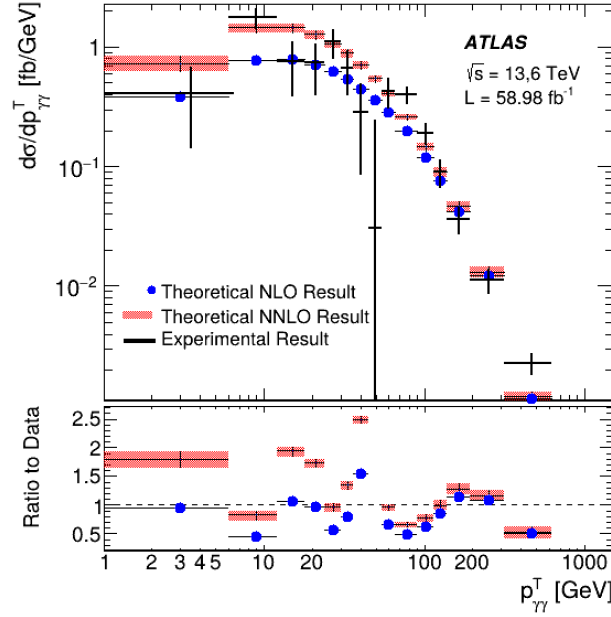


Figure 13: Differential cross section in logarithmic scale.

event selection cuts. In this project the efficiency was of 36,2 %, which is supposed to be maintained for the experimental data. Dividing the previous result by this amount will give the final total cross section of the Higgs boson production.

$$\sigma_{H_0 \rightarrow \gamma\gamma}^{exp} = \sum_i \left(\frac{d\sigma}{dp_{\gamma\gamma}^T} \right)_i \cdot (\Delta p_{\gamma\gamma}^T)_i$$

$$\sigma_{H_0} = \sigma_{H_0 \rightarrow \gamma\gamma}^{exp} \cdot \frac{1}{BR_{\gamma\gamma}(125 \text{ GeV})} \cdot \frac{1}{\eta_{cuts}} \quad (7)$$

The final result is $\sigma_{H_0} = 53 \pm 7 \text{ pb}$. This result is highly satisfactory as it is extremely close to the official result by the ATLAS Collaboration from 2024 and to the SM prediction ($59,9 \pm 2,6 \text{ pb}$). It is relevant to highlight that the uncertainty considered in this work is purely statistical, while the ATLAS Collaboration's result also includes systematic uncertainties.

By using the inclusive region (shown in Figure 11), the signal events can be quantified and divided by the total luminosity. This gives an inclusive total cross section of $\sigma_{inc}^{reco} = 46 \pm 6 \text{ fb}$. However, to compare with the theoretical Standard Model prediction, the unfolding factors that were calculated in Section 7.1 need to be used. As an estimation, an unfolding coefficient of $0,74 \pm 0,07$ is used¹⁵. Dividing by this coefficient, an inclusive total cross section is obtained: $\sigma_{inc}^{fid} = 62 \pm 10 \text{ fb}$. This result is in good agreement with the one obtained by the ATLAS Collaboration ($76_{-13}^{+14} \text{ fb}$), with the predicted by the state-of-the-art Standard Model calculations ($67,6 \pm 3,7 \text{ fb}$) [16] and with some of the most

¹⁵To obtain a better result, one should weight the relative importance of each unfolding coefficients for each $p_{\gamma\gamma}^T$ bin and obtain a much more precise value for the general coefficient, but as an estimation taking the simple average can work. The uncertainty comes from the quadrature sum of all the errors.

recent fiducial cross section measures for this process, made by the CMS Collaboration (Compact Muon Solenoid) in 2025 (74^{+16}_{-15} fb) [17].

9 Summary and Conclusion

The importance of studying the Higgs boson and its properties not only lies in increasing the precision of some of its intrinsic characteristic such as mass or life-time but also in obtaining a better understanding of several processes where it or its mechanism are involved.

In this project experimental events from proton proton collisions at LHC and measured by the ATLAS detector in 2022 and 2023 were used to study a specific decay channel for the Higgs boson (diphoton channel). Moreover, Monte Carlo simulations based on the Standard Model theory were used as a way to validate the theoretical predictions. Different methods currently used in the state-of-the-art HEP analysis were used such as the Spurious Signal Method in order to be able to detect the $H_0 \rightarrow \gamma\gamma$ signal from the thousands of background events present. To compare with theoretical predictions, an unfolding has been used on the experimental data.

The Higgs boson signal in the inclusive region was satisfactorily detected and a fiducial total cross section of 62 ± 10 fb was calculated, which agrees with the experimental result for the ATLAS Collaboration from 2024 (76^{+14}_{-13} fb) [16] and the theoretical prediction from the Standard Model ($67,6 \pm 3,7$ fb). The results are also in agreement with one of the latest measures from a high energy physics collaboration, in this case CMS, who obtained a fiducial total cross section of 74^{+16}_{-15} fb [17]. The differential cross section with respect to the $p_{\gamma\gamma}^T$ variable has also been calculated and compared to the theoretical prediction. Although the agreement here is worse due to statistical fluctuations, the overall behavior of both distributions is quite similar, and the results obtain match again with the experimental ATLAS Collaboration's results. Lastly, integrating the previous distribution in $p_{\gamma\gamma}^T$ the total cross section of a Higgs boson production was calculated, obtaining a final result of 53 ± 7 pb, again in agreement with the ATLAS experimental result of 58 ± 6 pb and with the SM prediction of $59,9 \pm 2,6$ pb.

Although this results are satisfactory, a lot of deeper study needs to be made in order to truly understand the physical implications of the Higgs boson, such as studying better event selection cuts or continue improving the precision of the differential cross section measures.

10 References

[1] P. Higgs. *Broken Symmetries and the Masses of Gauge Bosons*. Physics. Rev. Lett., 508-509 (1964).

- [2] F. Englert & R. Brout. *Broken Symmetry and the Mass of Gauge Vector Mesons*. Physics. Rev. Lett., 321-323 (1964).
- [3] The ATLAS Collaboration. *Observation of a New Particle in the Search for the Standard Model Higgs Boson with the ATLAS Detector at the LHC*. Physics Letters B. (2012)
- [4] The CMS Collaboration. *Observation of a new boson at a mass of 125 GeV with the CMS experiment at the LHC*. Physics Letters B. (2012).
- [5] S. Dawson, P. Meade, I. Ojalvo & C. Vernieri. *Report of the Topical Group on Higgs Physics for the Energy Frontier: The Case for Precision Higgs Physics*. 2-3 (2022).
- [6] The ATLAS Collaboration. (2014, July 14). *The Higgs boson's shadow*. Retrieved from atlas.cern: <https://atlas.cern/updates/briefing/higgs-boson-s-shadow>
- [7] The ATLAS Collaboration. *Measurements of the Higgs boson inclusive and differential cross-sections in the diphoton decay channel with pp collisions at $\sqrt{s} = 13$ TeV with the ATLAS detector*. (2022).
- [8] The ATLAS Collaboration. *Measurements of Higgs boson properties in the diphoton decay channel with 36 fb⁻¹ of pp collision data at $\sqrt{s} = 13$ TeV with the ATLAS detector*. (2019).
- [9] J. Terrón. *Seminarios de Introducción a TFG - Práctica del LHC*. (2021).
- [10] The ATLAS Collaboration. *Preliminary analysis of the luminosity calibration for the ATLAS 13.6 TeV data recorded in 2023*. 28 (2024).
- [11] The ATLAS Collaboration. ATLAS Note. *Measurements of Higgs boson coupling properties in the diphoton decay channel using full Run 2 pp collision data at $\sqrt{s} = 13$ TeV with the ATLAS detector*. (2023).
- [12] The ATLAS Collaboration. ATLAS Note. *Measurement of fiducial and differential cross sections in the $H \rightarrow \gamma\gamma$ decay channel with 139 fb⁻¹ of 13 TeV proton-proton collision data with the ATLAS detector*. (2022).
- [13] L. Dominguez. *Studies of photon isolation in a large-pileup environment and search for axion-like particles decaying into two photons with the ATLAS detector at the LHC*. 153 (2021).
- [14] A. Cueto. *Measurements of isolated-photon production inclusively and in association with jets at $\sqrt{s} = 13$ TeV with the ATLAS detector*. 23-30 (2018).

[15] CERN. *Sudakov Resummation*. (2019).

[16] The ATLAS Collaboration. *Measurement of the $H \rightarrow \gamma\gamma$ and $H \rightarrow ZZ^* \rightarrow 4\ell$ cross-sections in pp collisions at $\sqrt{s} = 13.6$ TeV with the ATLAS detector*. (2024).

[17] The CMS Collaboration. *Measurements of inclusive and differential Higgs boson production cross sections at $\sqrt{s} = 13.6$ TeV in the $H \rightarrow \gamma\gamma$ decay channel*. (2025).

[18] X. Chen, T. Gehrmann, E.W.N. Glover, A.Huss, B. Mistlberger & A. Pelloni. *Fully Differential Higgs Boson Production to Third Order in QCD*. (2021).

[19] G. P. Salam & E. Slade. *Cuts for two-body decays at colliders*. (2021).

[20] P. Kaffle, J. Huston & A. Tarek. *Update on optimal product cut value*. (2024).

11 Appendix

11.1 Appendix A. Product cuts

As commented in Sections 3 and 7.2.2, to predict the outcome of scattering events at the LHC a perturbative analysis is done. The improvement in experimental developments from the last few years has given high energy experimental physicist the ability of measuring observables with an extraordinary precision, demanding equally precise theoretical predictions in order to continue testing the Standard Model of particle physics. In the case of the Higgs boson production, where ggH is the dominant mechanism, N^3LO predictions have been made and even used to predict differential fiducial distributions (with respect to the rapidity¹⁶ magnitude) for the diphoton decay channel [18].

The methods followed to obtain the results are out of the scope of this work, but the predictions them self present an extremely interesting behavior. Usually, when theoretical physicists are able to go one order further in the perturbative analysis of QCD for the calculation of a differential cross section with respect to an specific magnitude, the corrections to the previous order is either constant or smooth across the magnitude. Thus, sometimes they can be modeled as the previous order prediction times a factor called K , which is usually defined as the ratio between the higher order inclusive cross section and the previous order one. In this case, as the new order is N^3LO , the factor is called K_{N^3LO} -factor [18].

To complete the theoretical predictions, the same event selection cuts that will be used experimentally need to be used here. The results for the distribution in rapidity of the Higgs boson and the distribution of the difference in rapidity for both produced photons are shown in Figure 14. As it can be seen, the N^3LO predictions do not follow the previously commented behavior of being just a scaling of the NNLO ones. Instead, they show an erratic conduct. In Figure 14a the ratio with respect to NNLO seems to vary quite notably depending on the rapidity value, and in Figure 14b this ratio almost triples for a certain rapidity value. Of course, this does not make any sense scientifically, and thus there must be a problem with the convergence of the perturbative series behind the calculus of these N^3LO prediction.

The origin of the instability shown in Figure 14b is traced back (in a non trivial manner) to the minimum p^T cut for the selected photons that was part of the event selection criteria (called ‘relative p^T cuts’).

At the end of the day, the relative p^T cut used to selected events is an arbitrary way of selecting photons which may be interesting for the study of this specific process. However, the functional form of this requirement is not crucial, and others might be used. One of the cuts that can be used is the ‘product cut’ [19], where instead of using two individual

¹⁶For massless particles, the rapidity matches the pseudorapidity defined in Section 2

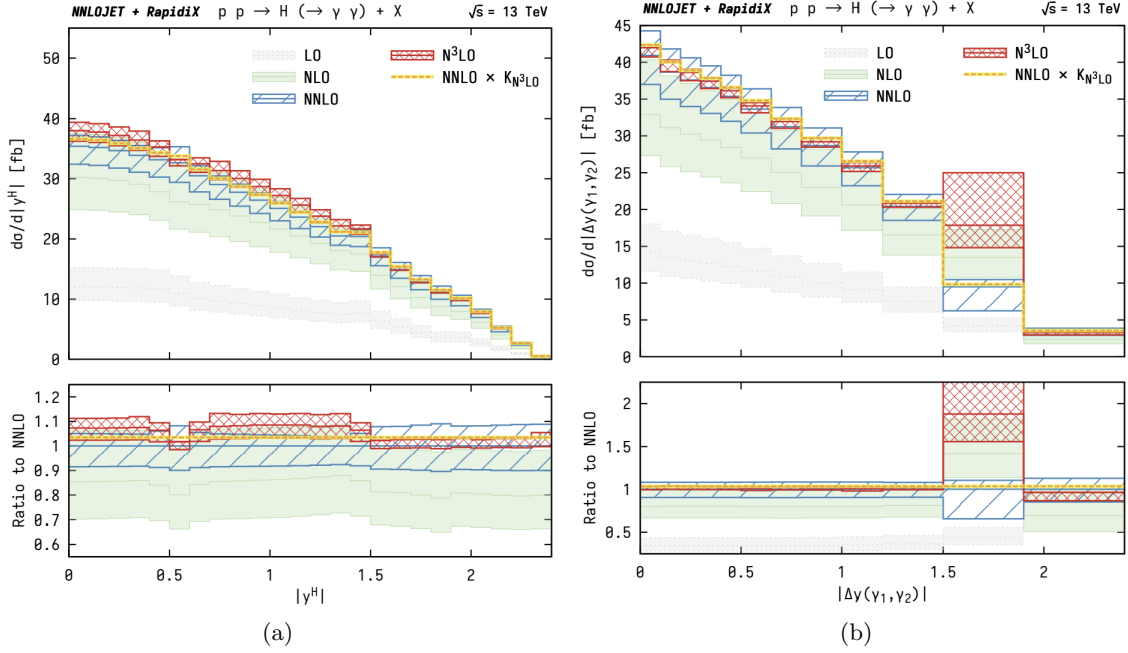


Figure 14: a) Fiducial differential cross section prediction for the rapidity distribution of the Higgs boson. b) Distribution for the absolute value of the difference in rapidities of the two produced photons. In both cases, predictions are shown at LO (gray), NLO (green), NNLO (blue), N^3LO (red) and NNLO scaled by the K_{N^3LO} -factor (orange). In both lower graphs, the ratio with respect to NNLO predictions is shown [18].

relative cuts for each photon, one maintains the relative for the subleading photon but substitutes the relative cut for the leading photon with an expression of the form:

$$\sqrt{p_{\gamma,l}^T \cdot p_{\gamma,s}^T} > \xi \cdot m_{\gamma\gamma} \quad (8)$$

where ξ is a certain arbitrary threshold. By using this cut instead of the relative one, the weird behaviors seen in Figure 14 are either gone or mostly reduced. Thus, regarding the theoretical predictions, this change could be highly beneficial. However, it is important to check whether this has a relevant impact in the event selection process experimentally, which will be briefly discussed now.

To find the parameter ξ that could give similar results to the ones already obtained, several ones were used in the ggH samples (as it is the most important production mode) and the most similar one was selected. The two magnitudes that were used to quantify the closeness between results was the cut efficiency and the purity, defined as:

$$Efficiency = \frac{\int ggH (SetCuts + ProductCut)}{\int ggH (SetCuts)}$$

$$Purity = \frac{\int ggH (SetCuts + ProductCut)}{\int Background (SetCuts + ProductCut)}$$

The integral sign makes reference to the number of events that pass the specified cuts. The ‘Set Cuts’ are all the cuts except the product cut. Thus, the efficiency of the cut measures how many signal events it is keeping and the purity is a measure of how many signal events pass the cuts in relation to the background events. If both the relative and product p^T cut are varied, the results of Figure 15 are obtained.

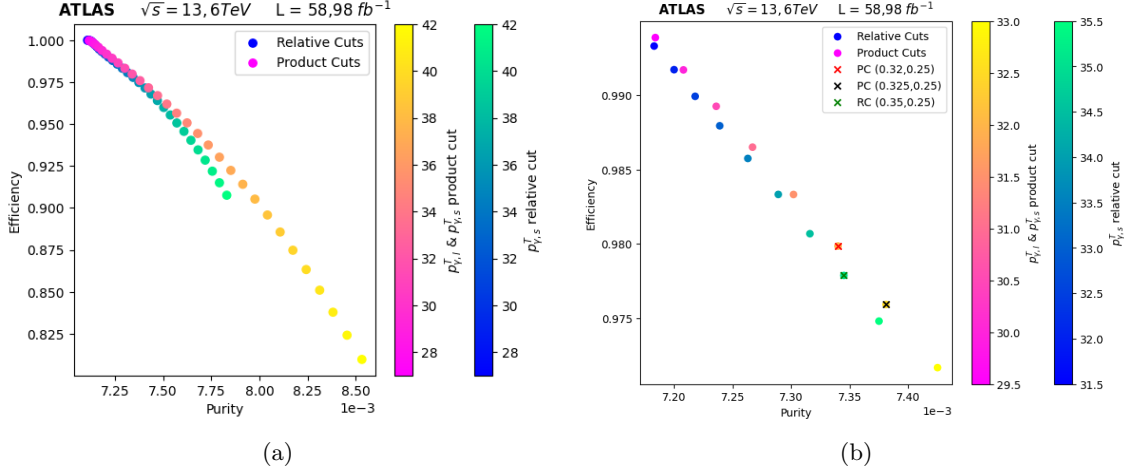


Figure 15: a) Efficiency and Purity results for the ggH simulations varying both the relative and the product p^T cut. b) Zoom of the results for the currently used relative cut and two possible product cut substitutes.

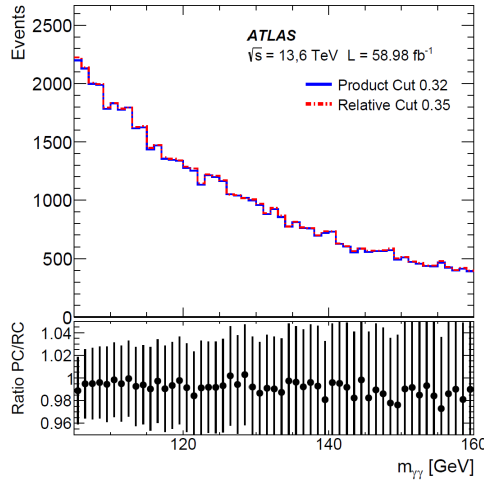


Figure 16: Ratio between the $m_{\gamma\gamma}$ distribution obtained using the 0.32 Product cut and the one obtained using the 0.35 original relative cut. The $p_{\gamma\gamma}^T$ of the events is in this case between 24 and 30 GeV.

As it can be seen, the efficiency and purity of both cuts are similar, although the case of product cuts can be even better as it lies above the relative cut curve. In Figure 15b, the currently used relative cut is signaled with a green cross while two possible product cut

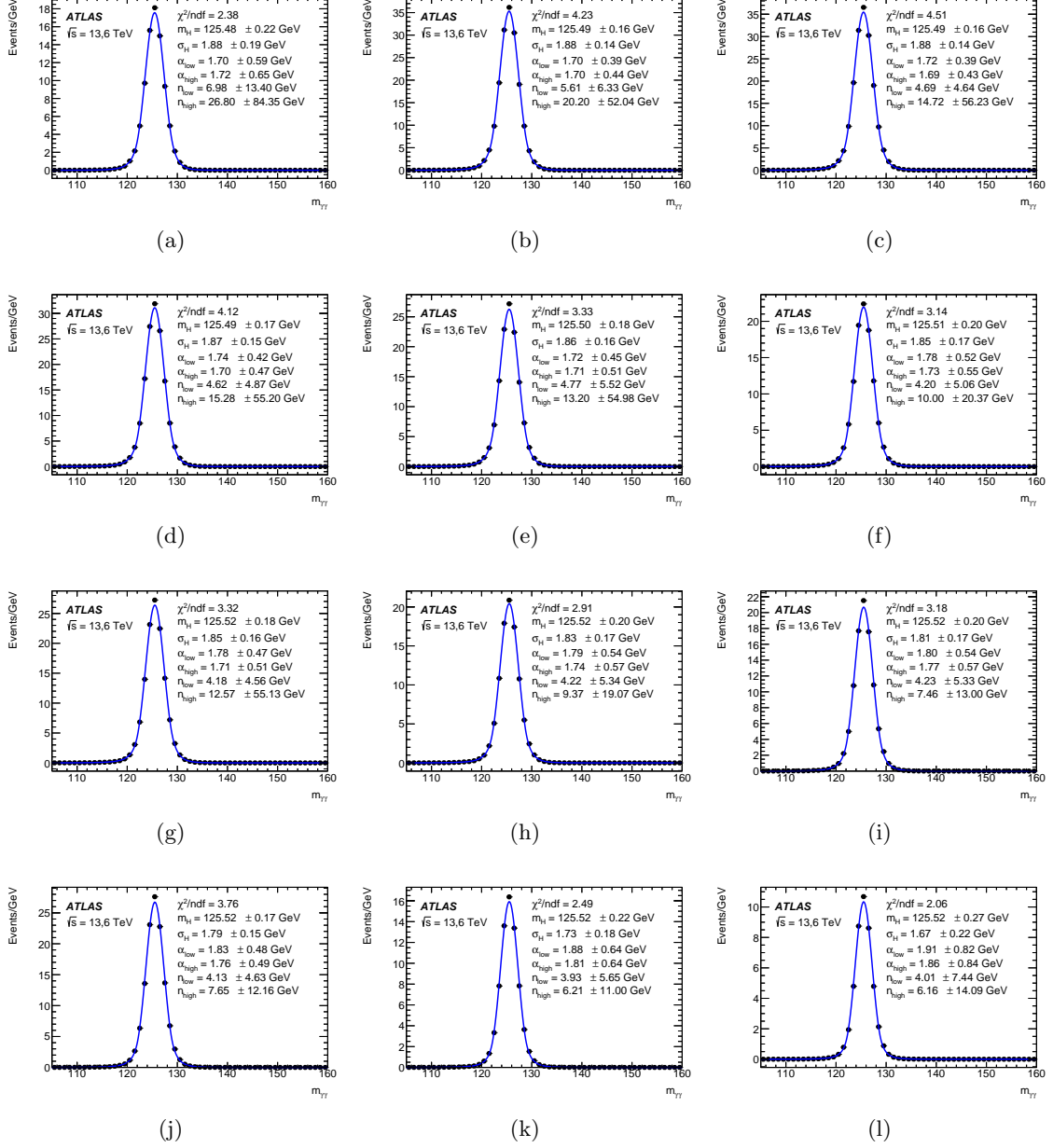
substitutes are also marked. The product cut of $\xi = 0.32$ is especially appealing as the efficiency improves in a bigger way than the purity gets worse [20]¹⁷. Figure 16 shows the effect that using one cut or another could have in an arbitrary $p_{\gamma\gamma}^T$ bin of the ones used during the work to calculate the differential cross section.

It can be seen that the differences between them are quite low, with the ratio between them ranging from 0,95 to 1,05. Thus, it can be concluded that they change from using two relative p^T cuts to using one relative cut and another product cut should not have a relevant effect regarding the experimental concerns but could actually help to make better theoretical predictions when calculating them at high orders of the perturbative QCD analysis.

¹⁷Other production modes such as VBF and ttH were studied. In these cases, both the efficiency and the purity were slightly worse than with the original relative cut. However, the differences were always lower than 0,03% for the efficiency and 0,3% for the purity.

11.2 Appendix B. Monte Carlo signal fitting results

In these appendix the results for the Monte Carlo signal modeling for each $p_{\gamma\gamma}^T$ bin are shown.



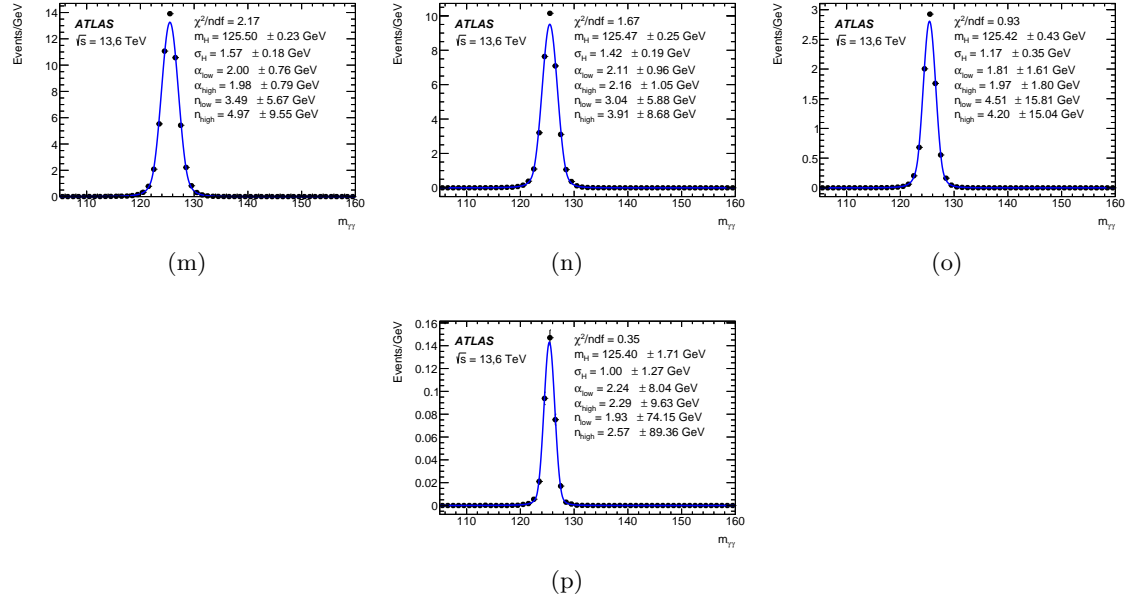


Figure 16: a) stands for bin 0, b) stands for bin 1 and so on until p), which stands for the 16th bin.

11.3 Appendix C. Example of Spurious Signal method

In this Appendix, the result of the Spurious Signal method analysis for an arbitrary bin (in this case bin 9, where $66 < p_{\gamma\gamma}^T < 90$ GeV events are stored) are shown (Figure 17). In this specific case, the *Power* and the *ExpPol1* functions are less precise and the other three do a great job fitting the background-only distribution. As all of them satisfy the criteria, the function with less free parameter, in this case *ExpPol2* is chosen.

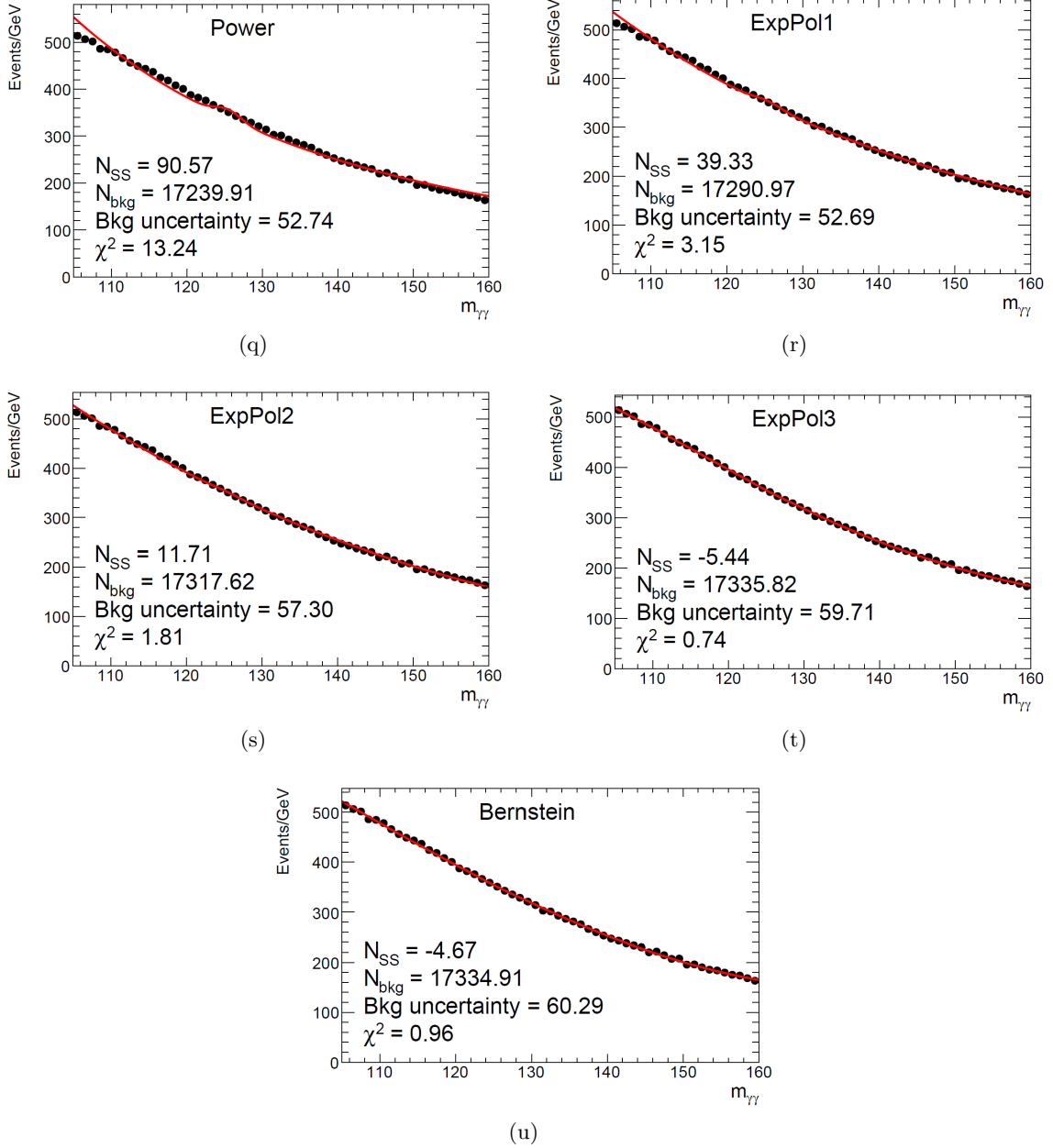
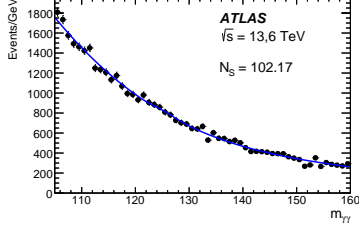


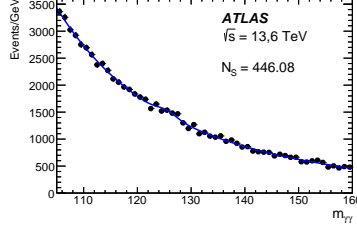
Figure 17: a) Power function results. b) Exponential of a first degree polynomial results. c) Exponential of a second degree polynomial results. d) Exponential of a third degree polynomial results. e) Bernstein polynomial results.

11.4 Appendix D. Data fitting results

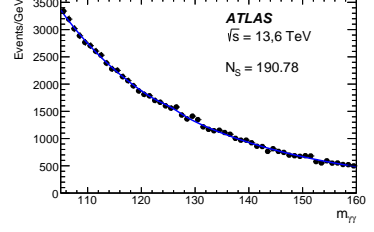
In this appendix the fitting results of the background and signal functions for each $p_{\gamma\gamma}^T$ data bin are shown.



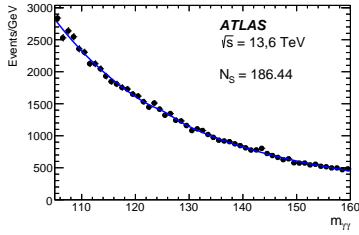
(a)



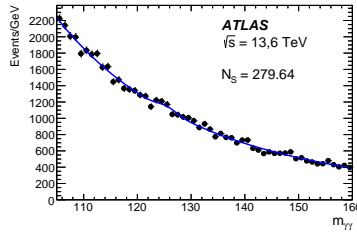
(b)



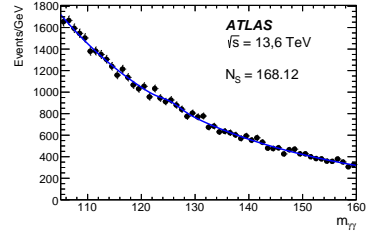
(c)



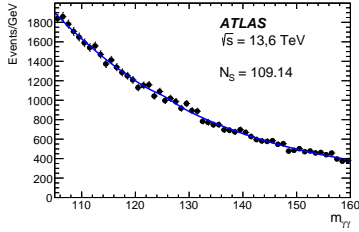
(d)



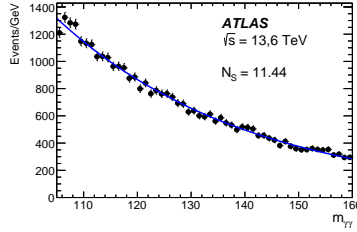
(e)



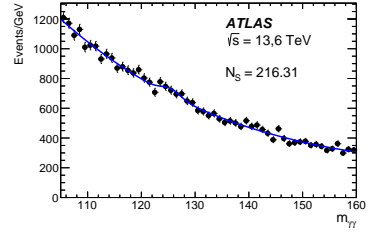
(f)



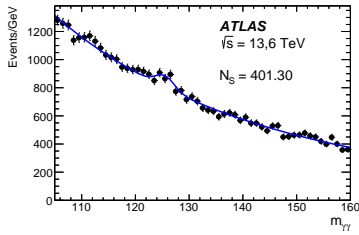
(g)



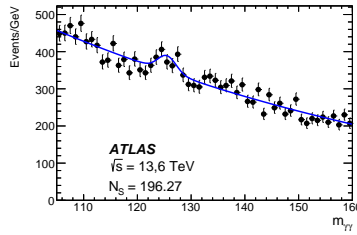
(h)



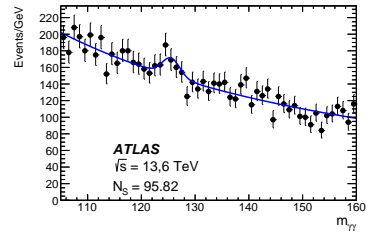
(i)



(j)



(k)



(l)

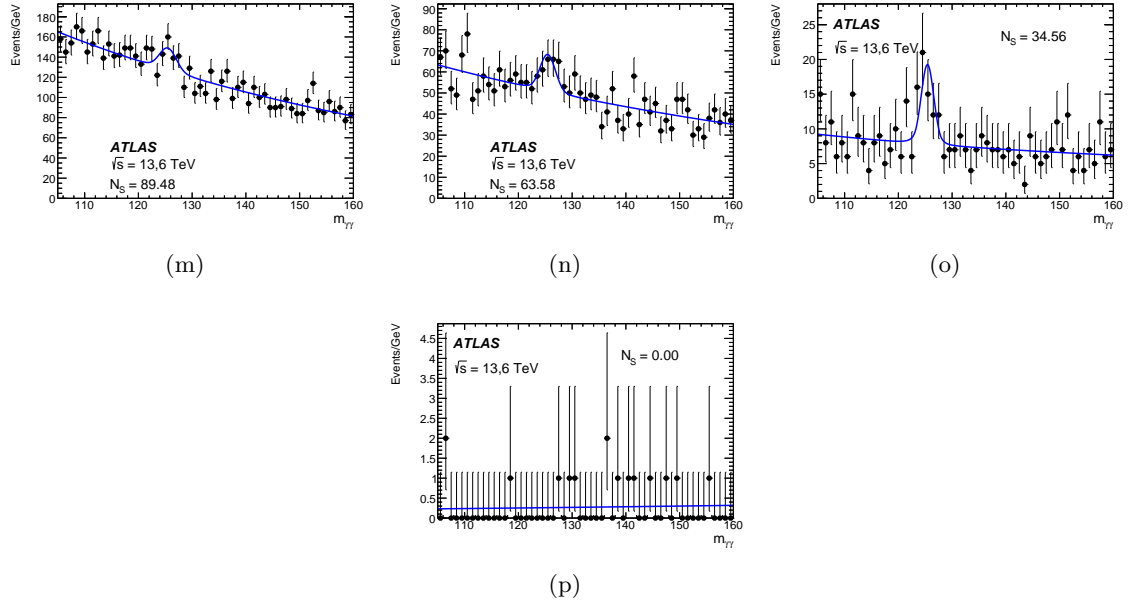


Figure 17: a) stands for bin 0, b) stands for bin 1 and so on until p), which stands for the 16th bin.

11.5 Appendix E. Comparison between NLO and NNLO

As shown in Figure 12 and Figure 13, the NLO and NNLO predictions differ substantially. The most important difference is that the NLO prediction for the differential cross section is much lower than the NNLO prediction. This shows the need of including the NNLO terms in the Monte Carlo calculations, as they will consider higher order processes which are indeed still contributing notably to the process cross section.

The second difference is harder to recognize and it is related to the shape of the distribution. To better study this, both distributions have been normalized and shown in Figure

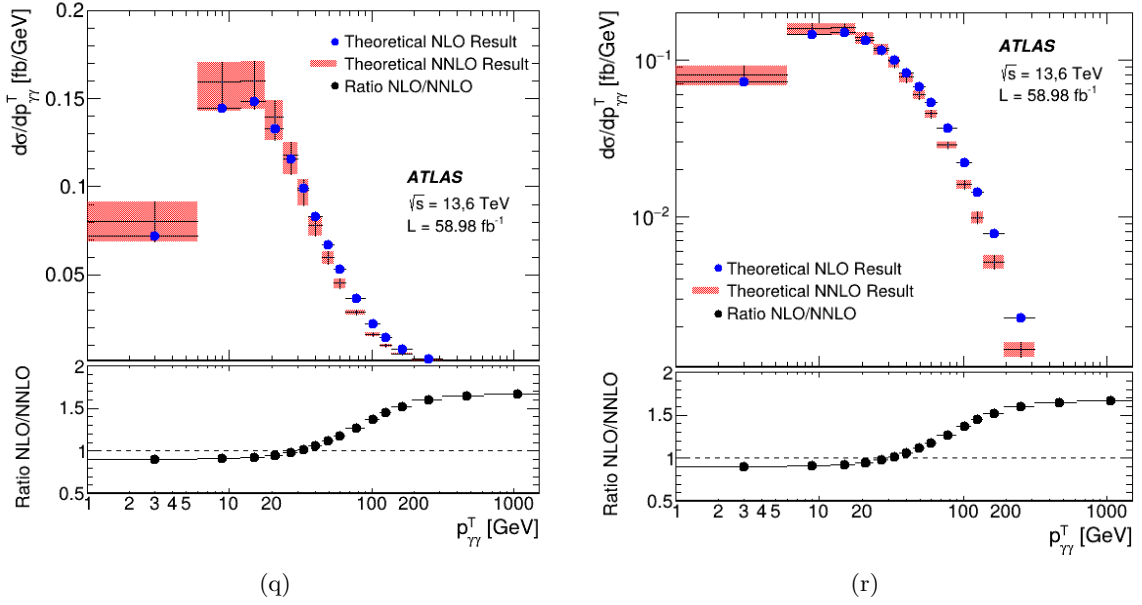


Figure 18: a) NNLO and NLO differential cross section predictions normalized and the ratio between them. b) NNLO and NLO differential cross section and their ratio in logarithmic scale.

By looking at both graphs above, it can be seen that the shapes are slightly different, especially at high values of $p_T^{\gamma\gamma}$, where the NLO distribution has a bigger tail, whose origin lies in the fact that the NLO calculations assume infinite mass for the top quark while the NNLO calculations do not. This is the reason behind the apparent convergence of NLO and NNLO in the differential cross section of Figure 13. As the normalization is smaller for the NLO distribution, the crossing between them happens at higher $p_T^{\gamma\gamma}$ than in the case shown above, where the ratio between them surpasses unity at less than 30 GeV.